



# Effect of nitrogen-containing polymer wrapped around carbon nanotubes for Li–O<sub>2</sub> battery cathode

Tsuyohiko Fujigaya<sup>1,2,3,4</sup> · Ryota Kanamori<sup>1</sup> · Shinsuke Hirata<sup>1</sup> · Junichi Morita<sup>1</sup> · Masamichi Matsumoto<sup>1</sup> · Masato Eguchi<sup>1</sup> · Il-Chan Jang<sup>1</sup> · Tatsumi Ishihara<sup>1,2</sup> · Naotoshi Nakashima<sup>2</sup>

Received: 24 February 2019 / Revised: 13 April 2019 / Accepted: 15 April 2019 / Published online: 27 May 2019  
© The Society of Polymer Science, Japan 2019

## Abstract

In the development of lithium (Li)–oxygen (O<sub>2</sub>) rechargeable batteries, the improvement of the rechargeability is one of the key issues to be solved. Herein, a novel strategy to solve this issue is explored using polymer-wrapped single-walled carbon nanotubes (SWCNTs) as the cathode material. Poly[2,2'-(2,6-pyridine)-5,5'-bibenzimidazole] (PyPBI), employed as the wrapping polymer of the SWCNTs, served to coordinate Li ions and to facilitate a favorable deposition of the discharge products on the SWCNTs during the discharge reaction at the cell cathode. As a result, the rechargeability of the cell (SWCNT/PyPBI-cell) was improved compared to the cell having nonwrapped SWCNTs as the cathode (SWCNT-cell).

## Introduction

Nonaqueous lithium (Li)–oxygen (O<sub>2</sub>) batteries have attracted significant attention as a promising rechargeable battery due to their highest theoretical specific energy (11428 Wh kg<sup>-1</sup> when excluding O<sub>2</sub> mass) [1–6]. In the nonaqueous Li–O<sub>2</sub> battery, the Li ions delivered from the anode react with O<sub>2</sub> (air) and electrons as  $2\text{Li}^+ + \text{O}_2 + 2\text{e}^- \rightarrow \text{Li}_2\text{O}_2$  [2, 7]. The battery shows a rechargeability since the reaction is reversible. The Li–O<sub>2</sub> batteries possess an exceptionally high-energy density since (1) Li metal has the lowest atomic mass and a low electronegativity (–3.04 V vs. SHE

(Standard Hydrogen Electrode)) among all solid electrode materials, and (2) O<sub>2</sub> is abundantly stored in the surrounding environment. Critical problems in the current system include (1) the low specific energy density of the cell compared to the theoretical values, (2) the large overpotential (especially for the charging process), and (3) the poor discharge–charge repeatability (rechargeability). The reasons for these issues include the stability of the electrolyte and the nature of the discharge products [8, 9]. Especially, since the Li<sub>2</sub>O<sub>2</sub> is an insoluble and insulating material and deposits as micron-size particles [10], the clogging of the cathode occurs, which prevents the diffusion of the electrolyte and O<sub>2</sub>, limits the capacity [11] and increases the charging overpotential [12, 13]. As a result, the cell loses its rechargeability.

To overcome these issues, developments in a novel cathode that can accommodate a substantial amount of Li<sub>2</sub>O<sub>2</sub> were designed [14–19]. Along this line, carbon nanotubes (CNTs) were extensively investigated as a replacement for the typical electrode based on carbon black (CB) since CNTs can form a continuous porous network with a stiff structure in the absence of binder materials [20–23]. However, an investigation into the control of the discharge product using a CNT cathode has not been carried out.

In this study, we propose a polymer coating for CNTs as a novel electrode in which a homogenous and ultrathin polymer layer is wrapped around the CNT surface to facilitate a favorable deposition of the discharge products by

**Supplementary information** The online version of this article (<https://doi.org/10.1038/s41428-019-0207-2>) contains supplementary material, which is available to authorized users.

✉ Tsuyohiko Fujigaya  
fujigaya.tsuyohiko.948@m.kyushu-u.ac.jp

- 1 Department of Applied Chemistry, Graduate School of Engineering, Kyushu University, 744 Motoooka, Nishi-ku, Fukuoka 819-0395, Japan
- 2 International Institute for Carbon Neutral Energy Research (WPI-I2CNER), Kyushu University, Fukuoka 819-0395, Japan
- 3 Japan Science and Technology Agency-PRESTO, 4-1-8 Honcho, Kawaguchi, Saitama 332-0012, Japan
- 4 Center for Molecular Systems (CMS), Kyushu University, 744 Motoooka, Nishi-ku, Fukuoka 819-0395, Japan

the affinity of  $\text{Li}^+$  toward the wrapped polymer. As the coating polymer, we chose poly[2,2'-(2,6-pyridine)-5,5'-bibenzimidazole] (PyPBI; Fig. 1a) since (1) we found that PyPBI can coat CNT surfaces homogeneously with a thickness of  $\sim 1$  nm [24–27], and (2) it is expected to promote the formation of the discharge products through the coordination of  $\text{Li}^+$  to the PyPBI ligand, which leads to a favorable deposition of the discharge products.

## Experimental procedure

### Materials

*N,N*-dimethylacetamide (DMAc); ethylene carbonate (EC), lithium battery grade; diethyl carbonate (DEC), lithium battery grade; lithium bis(trifluoromethanesulfonyl)imide (LiTFSI), lithium battery grade; and tetraethylene glycol dimethyl ether (TEGDME), lithium battery grade were purchased from Kishida Chemical Co., Ltd. Concentrated hydrochloric acid (HCl), methanol, and 2-propanol were purchased from FUJIFILM Wako Pure Chemical Industries, Ltd. The single-walled carbon nanotubes (SWCNTs,  $\sim 2$  nm in diameter) were purchased from Meijo Nanocarbon, Ltd. Poly[2,2'-(2,6-pyridine)-5,5'-bibenzimidazole] (PyPBI) was synthesized according to a previously reported method [28].

### Material characterization

X-ray photoelectron spectroscopy (XPS) and SEM images were measured using an AXIS-ULTRA<sup>DL</sup> (Shimadzu Corporation) and SU9000 (Hitachi High-tech), respectively. The specific surface area and micropore distribution were determined by the Brunauer–Emmett–Teller (BET) method

and Horvath–Kawazoe (HK) method (applying the carbon- $\text{N}_2$  interaction parameter at 77 K), respectively, as based on the  $\text{N}_2$  adsorption isotherm measurements (77 K,  $10^{-8} < P/P_0 < 1$ ) using a BELSORP-max (BEL Japan, Inc.) instrument that was upgraded by changing the connection of the sample tube to a VCR<sup>®</sup> metal gasket to avoid gas leakage and to measure pressures as low as  $P/P_0 = 10^{-8}$  to  $10^{-6}$ , which correspond to the micropore region. The gas adsorption measurements were conducted under high vacuum after a pretreatment at 150 °C for over 12 h. X-ray diffraction (XRD) was performed by a SmartLab (Rigaku) with a plastic bag to protect the cathodes from moisture.

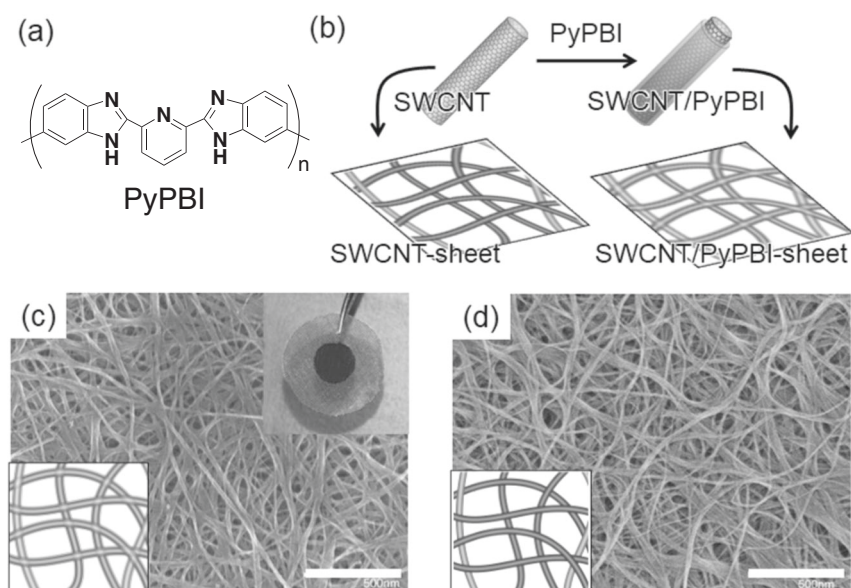
### Purification of SWCNT

A 50-mg portion of the as-produced SWCNTs was heated at 450 °C in air for 15 min in order to remove any amorphous carbon. The obtained powder was then shaken in aq. HCl (2.0 M) at room temperature for 2 h to remove any metal impurities. These procedures were repeated one more time.

### Synthesis of SWCNT/PyPBI

The SWCNTs wrapped by the PyPBI (denoted SWCNT/PyPBI) were prepared according to our previous method [29]. Briefly, the purified SWCNTs (7.0 mg) were added to a DMAc solution (25.0 mL) of PyPBI (15.0 mg) and then sonicated for 20 min using a probe-type sonicator (UD-200, TOMY SEIKO Co., Ltd.). The dispersion was then centrifuged at  $5000 \times g$  for 1 h (Himac CS100 GXL, HITACHI Koki Co., Ltd.), and the supernatant was filtered using a PTFE filter (100-nm pore size, ADVANTEC), followed by vigorous washing with DMAc to remove any unbound PyPBI. After washing with methanol and drying under

**Fig. 1** **a** Chemical structure of PyPBI. **b** Schematic illustration of the preparation of the SWCNT sheet and SWCNT/PyPBI sheet. SEM images of the **c** SWCNT/PyPBI sheet and **d** SWCNT sheet as cathodes. Scale bars; 500 nm. Inset: photo of the cathode fabricated with the SWCNT/PyPBI sheet on a SUS sheet



vacuum, the SWCNT/PyPBI was obtained as a black powder (3.5 mg).

### Preparation of SWCNT/PyPBI electrode

The electrodes were prepared using a filtration method. The SWCNT/PyPBI (0.8 mg) was dissolved in DMAc (3.0 mL) and then sonicated for 1 h using a bath-type sonicator (Branson 5510). The obtained solution was then slowly casted on an SUS mesh (SUS316, 100 mesh). After washing with methanol, the electrode was dried under vacuum at 160 °C. In a similar manner, a control electrode (SWCNT-electrode) having no PyPBI was prepared from the SWCNTs (0.8 mg) dispersed in DMAc. No binder was used during the electrode fabrication processes.

### Electrochemical measurement

The electrode was pressed onto a stainless steel mesh, and the cathode was dried in a vacuum oven at 160 °C for 9 h. Lithium foil (thickness: 0.1 mm, Shinji Metallic Co., Ltd.) was used as the anode and was separated from the cathode by two pieces of a glass fiber separator (GA-200,  $\Phi = 26$  mm, ADVANTEC). A mixed solution of EC and DEC (3:7 = vol/vol) or TEGDME containing 1.0 M LiTFSI was used as the electrolyte. All the cells were gas-tight sealed except for the stainless steel mesh window used to admit 1 atm of oxygen gas. Discharge–charge measurements were performed in the voltage range of 4.5–2.0 V at a current density of 0.1 mA cm<sup>-1</sup>. For the SEM observations of the electrodes after the discharge–charge measurements, the disassembled electrode was washed with DEC, dried under vacuum, and then mounted on an SEM holder in the glove box under a nitrogen atmosphere.

## Results and discussion

### Characterization of SWCNT/PyPBI

For the CNTs, we used single-walled carbon nanotubes (SWCNTs) due to their specific surface area being higher than that of multi-walled carbon nanotubes (MWCNTs), which can lead to a higher specific capacity [20]. PyPBI-coated SWCNTs (SWCNT/PyPBI, Fig. 1b) were prepared according to our previous report [28]. The SWCNTs were sonicated in a DMAc solution of PyPBI for 60 min, which were filtered and vigorously washed with DMAc to remove any unbound PyPBI from the composite. The composition ratio determined by elemental analysis was SWCNT:PyPBI = 64:36 (in weight). Based on this result together with the Brunauer–Emmett–Teller (BET) surface area of the SWCNTs (810 m<sup>2</sup> g<sup>-1</sup>) determined from the N<sub>2</sub> adsorption

measurements and the density of the PyPBI (1.33 g cm<sup>-3</sup>) [30], the thickness of the coating polymer layer was calculated to be ca. 0.5 nm. The value is almost comparable to that of the PyPBI coating on MWCNTs in which the homogeneous coating was well visualized by SEM observation [31]. Fig. 1c, d shows SEM images of the electrode fabricated on an SUS mesh in which SWCNT/PyPBI (Fig. 1c) was placed by a filtration method. A control electrode using the nonwrapped SWCNTs was also fabricated (Fig. 1d) in a similar manner. For both electrodes, fibrous network structures were formed. As seen in the inset of Fig. 1c, the fabrication of the electrode film was possible without using any binder materials due to the stiff entanglement of the fibrous SWCNTs, which is favorable for increasing the specific capacity of the cell.

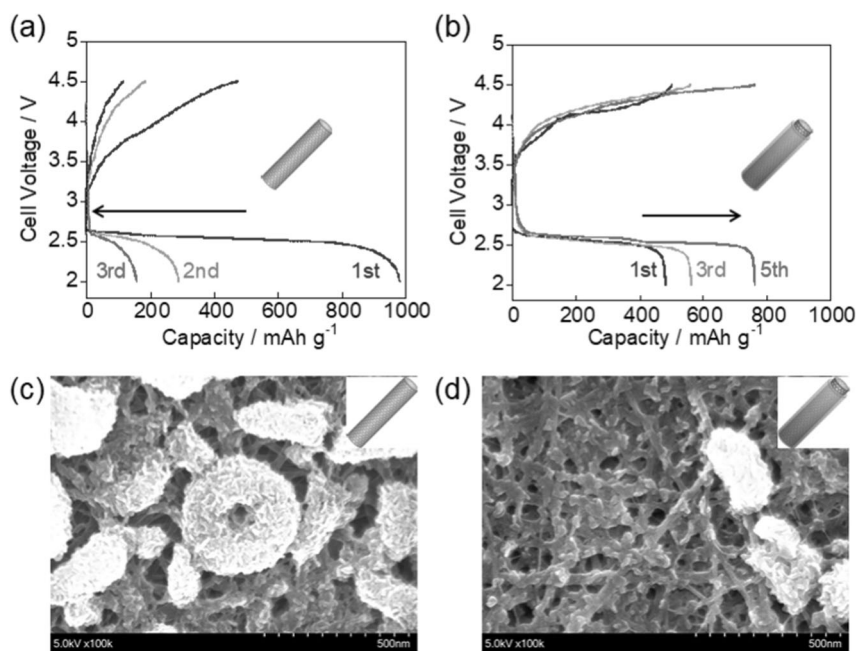
The SWCNT sheet showed a slightly higher BET surface area (294 m<sup>2</sup> g<sup>-1</sup>) than that of SWCNT/PyPBI (242 m<sup>2</sup> g<sup>-1</sup>) [32]. It is noted that these values were significantly smaller than that of as-grown SWCNT powder (810 m<sup>2</sup> g<sup>-1</sup>). Most likely, the preparation of the sheet by the vacuum filtration method resulted in the close packing and bundling of the tubes, leading to the large decrease in the surface area.

### Cell performance

Figure 2 shows the typical discharge–charge curves of the cells using SWCNTs (SWCNT-cell, Fig. 2a) and SWCNT/PyPBI (SWCNT/PyPBI-cell, Fig. 2b) as the cathode electrodes. The measurements were carried out using TEGDME containing 1.0 M LiTFSI as the electrolyte at a current density of 0.1 mA cm<sup>-2</sup> and voltage cut-offs of 2.0 and 4.5 V vs. Li/Li<sup>+</sup>. TEGDME was used since ether-based solvents are more stable than carbonate-based solvents, such as ethylene carbonate (EC) and diethyl carbonate (DEC) [33, 34], and Li<sub>2</sub>O<sub>2</sub> is the predominant discharge product [35]. In the 1st discharge, the capacity of the SWCNT-cell (980 mAh g<sup>-1</sup>) was higher than that of the SWCNT/PyPBI-cell (480 mAh g<sup>-1</sup>). On the other hand, in the 1st charging, the capacity of the SWCNT-cell significantly dropped to 420 mAh g<sup>-1</sup>, while that of the SWCNT/PyPBI-cell (480 mAh g<sup>-1</sup>) was comparable. After the 1st cycle, the discharge capacity of the SWCNT-cell dropped, while that of the SWCNT/PyPBI-cell kept increasing and reached 850 mAh g<sup>-1</sup> after ten cycles (Fig. S1).

To explore the origin of this difference, ex situ SEM images of the cathodes of the two cells were measured after the 1st discharge since the importance of the Li<sub>2</sub>O<sub>2</sub> morphology in influencing the performance in terms of discharge capacity and rechargeability has been well discussed [8, 36, 37]. In the SWCNT-cell, we found that the cathode surface was fully covered by the discharge product and that large toroid particles characteristic of the Li<sub>2</sub>O<sub>2</sub> [16, 38] had been deposited (Fig. 2c), while for the SWCNT/PyPBI-cell,

**Fig. 2** Charge–discharge profiles of the (a) SWCNT-cell and (b) SWCNT/PyPBI-cell in TEGDME between 2.0–4.5 V (vs.  $\text{Li}/\text{Li}^+$ ) at a current density of  $0.1 \text{ mA cm}^{-2}$ . Only selected cycles are displayed for clarity. All the specific capacities are per gram unit of total electrode weight (i.e., SWCNTs and SWCNT/PyPBI for the SWCNT-cell and SWCNT/PyPBI-cell, respectively). SEM images of the (c) SWCNT-cell and (d) SWCNT/PyPBI-cell as cathodes after the 1st discharge. For lower magnification images, see Fig. S2



a fibrous structure coated with depositions (Fig. 2d) together with the  $\text{Li}_2\text{O}_2$  toroid particles was observed (for lower magnification images, see Fig. S2). The formation of  $\text{Li}_2\text{O}_2$  in the cells was also supported by the X-ray diffraction (XRD) measurements showing the characteristic (100), (101) and (110) (JCPDS No. 09-0355) (Fig. S3). Since the formation of the toroidal morphology is beneficial to the diffusion of oxygen and to increase the discharge capacity, the larger discharge capacity of the SWCNT-cell was explained by the differences in the  $\text{Li}_2\text{O}_2$  morphology. However, we assumed that the insulating  $\text{Li}_2\text{O}_2$  toroid particles were too large to decompose during the charging of the SWCNT-cell, resulting in an incomplete charging with a high overpotential (Fig. 2a). On the other hand, the quantitative discharging–charging of the SWCNT/PyPBI-cell in the 1st cycle (Fig. 2b) indicated the smooth decomposition of the discharge products due to the preferential formation of small discharge products during the 1st discharging. The increase in the capacity of the SWCNT/PyPBI-cell in the 2nd discharge was probably the result of an increase in the contact interface between the electrolyte and the PyPBI-wrapped SWCNT surface due to wetting, and this action increased the surface available for the deposition, as reported in the other systems [39]. The importance of such electrolyte filling was also pointed out by Zhang et al. [40]. Similar phenomena were also observed when EC/DEC was used as the solvent (Fig. S4).

To compare the behaviors of the cells with the same discharge/charge capacity, the rechargeability of the SWCNT-cell and SWCNT/PyPBI-cell cycled at a cutoff capacity of  $300 \text{ mAh g}^{-1}$  was tested (Fig. 3a, b). In the first charging of the SWCNT/PyPBI-cell, we observed a clear

two-step potential increase (below 4.0 V and above 4.0 V), while the SWCNT-cell exhibited a gradual increase, which is also presented in Fig. 2. In the two-step increase, the lower potential region was assigned to delithiation and disproportionation reactions ( $\text{Li}_2\text{O}_2 \rightarrow \text{LiO}_2 + \text{Li}^+ + \text{e}^-$  and  $\text{LiO}_2 + \text{LiO}_2 \rightarrow \text{Li}_2\text{O}_2 + \text{O}_2$ ), and the higher potential region was assigned to the bulk oxidation of  $\text{Li}_2\text{O}_2$  ( $\text{Li}_2\text{O}_2 \rightarrow 2\text{Li}^+ + \text{O}_2 + 2\text{e}^-$ ) [38, 41–43]. The difference in the shapes often originated from the morphology difference of the discharge products [43, 44], and the results indicated the PyPBI layer supported the formation of a more favorable morphology of  $\text{Li}_2\text{O}_2$  for charging. Indeed, in the SEM images of the SWCNT-cell and SWCNT/PyPBI-cell after the first discharge, the cathode surface was fully covered by thin plates with large particles for the SWCNT-cell (Fig. 3c), while a fibrous structure, with fibers thicker than the original fiber diameter (Fig. 1d), was clearly observed for the SWCNT/PyPBI-cell (Fig. 3d). Mitchell et al. [45] reported that  $\text{Li}_2\text{O}_2$  thin plates were formed first on CNTs, and then, the secondary nucleation of new plates eventually developed into a toroidal shape, which was comparable to the morphology observed for the SWCNT-cell. We considered that in the SWCNT-cell, the  $\text{Li}_2\text{O}_2$  was deposited preferentially on the cathode surface due to nucleation at the surface (Fig. 3e), whereas a homogeneous deposition occurred on not only the sheet surface but also the deeper sites for the SWCNT/PyPBI-cell due to the better wettability, as illustrated in Fig. 3f.

The capacities of the SWCNT-cell (Fig. 3g) and SWCNT/PyPBI-cell (Fig. 3h) were plotted as a function of the cycle number. We achieved a constant discharge capacity for the SWCNT/PyPBI-cell until the 50th cycle



**Fig. 3** Charge–discharge profiles of the (a) SWCNT-cell and (b) SWCNT/PyPBI-cell in TEGDME between 2.0–4.5 V (vs.  $\text{Li}/\text{Li}^+$ ) at a current density of  $0.1 \text{ mA cm}^{-2}$  for the 1st, 5th, 10th, 15th, 20th, 25th, and 30th cycles. The capacities were limited to  $300 \text{ mAh g}^{-1}$ . All the specific capacities are per gram unit of total sample weight. SEM images of the (c) SWCNT-cell and (d) SWCNT/PyPBI-cell cathodes after the 1st discharge. Scale bars: 500 nm. Schematic illustrations of the  $\text{Li}_2\text{O}_2$  deposition for the (e) SWCNT-cell and (f) SWCNT/PyPBI-cell. Plots of the capacity from charge–discharge cycles as a function of cycle number for the (g) SWCNT-cell and (h) SWCNT/PyPBI-cell in TEGDME between 2.0–4.5 V (vs.  $\text{Li}/\text{Li}^+$ ) at a current density of  $0.1 \text{ mA cm}^{-2}$

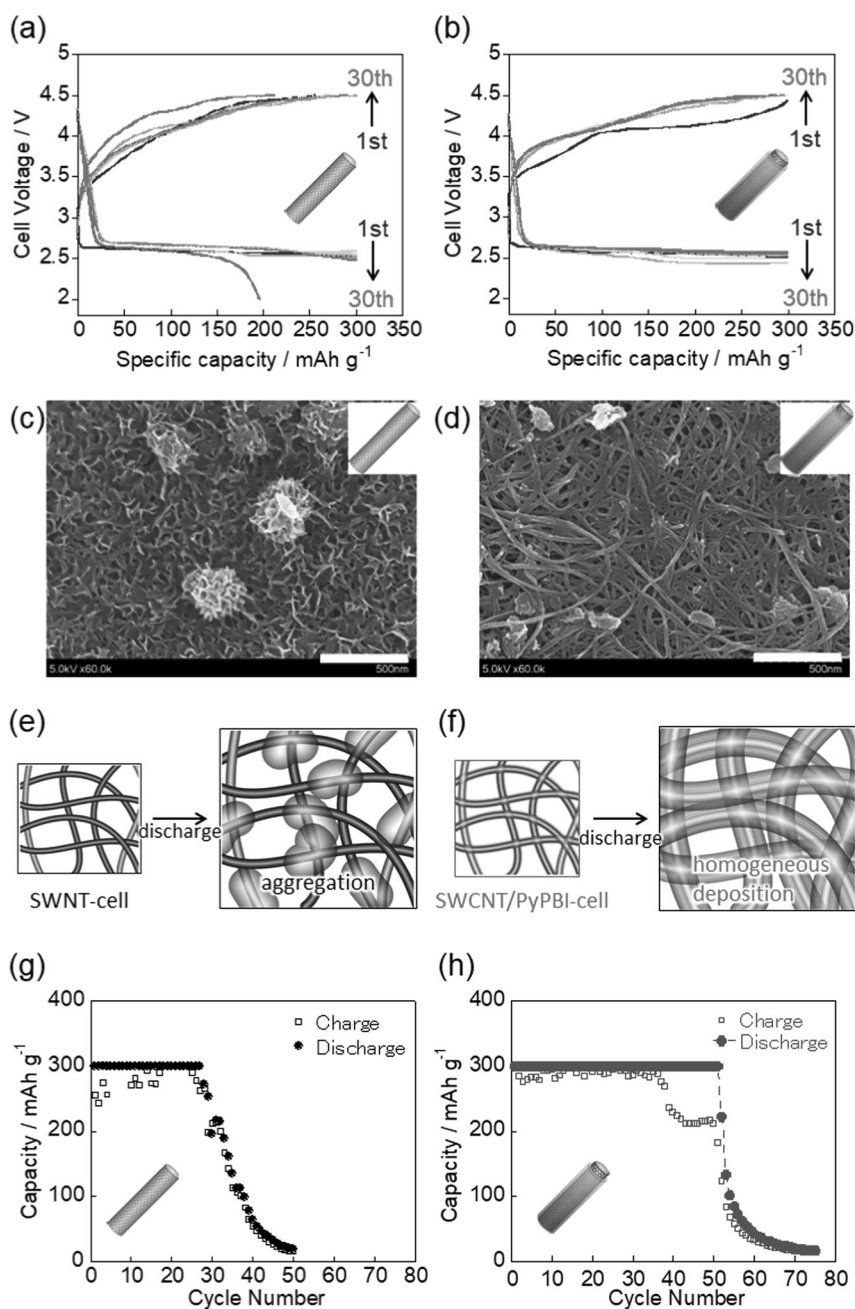


(Fig. 3g), whereas the capacity of the SWCNT-cell decreased after the 25th cycle (Fig. 3h). This deterioration in the capacity before the cycle limitation (40–50 cycles for charging in Fig. 3h) was often observed, indicating that the discharge product was not sufficiently oxidized probably due to the accumulation of the discharge product in the cathode. A similar superiority of the SWCNT/PyPBI-cell was also observed when the cell capacity was not limited (Fig. S1). We assumed that the homogenous deposition in the SWCNT/PyPBI-cell enabled the good rechargeability compared to that of the SWCNT-cell, in which preferential deposition on the cathode surface occurred.

The question remained as to the reason why the PyPBI coating enabled the better wettability and more favorable deposition. To investigate the mechanism, XPS narrow scans of the N 1s region of SWCNT/PyPBI before and after the discharge–charge test were measured (Fig. 4). Interestingly, the two peaks at 398.0 and 400.3 eV observed for the SWCNT/PyPBI before the test (black line) changed to a single peak at 399.5 eV after the test (red line), which was similar to the metal coordination on PyPBI (Fig. S5). Of further note is that the peak profile returned to its initial shape by washing the cathode with water (blue line). This result indicated the weak coordination of  $\text{Li}^+$  to PyPBI.

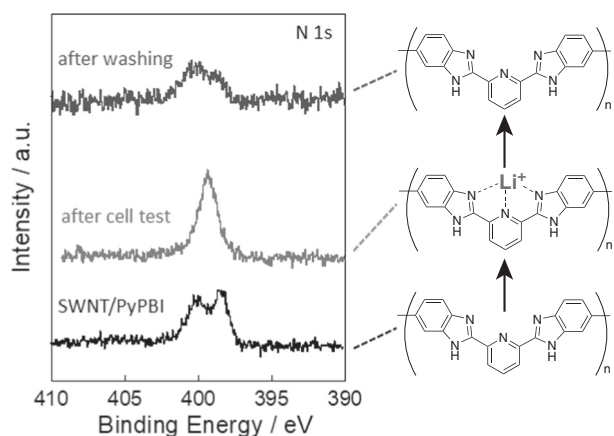


**Fig. 4** a X-ray photoelectron spectroscopy (XPS) N 1s narrow scans of SWCNT/PyPBI (black line), SWCNT/PyPBI after the cell test (red line), and SWCNT/PyPBI after washing with water (blue line). Proposed chemical structures of PyPBI upon discharge are also displayed

Zundel and coworkers [46] reported the coordination of  $\text{Li}^+$  to the pyridine-based ligand, which supports the complex formation of  $\text{Li}^+$  and PyPBI, as proposed in Fig. 4. Furthermore, on a graphitic surface, such as the CNT surface, the discharge intermediate product is able to migrate away from the charge transfer centers and settle at the structural defect sites, thus, forming large aggregates [47, 48]. Based on the above facts, we considered that the homogeneous PyPBI layer acted as binding sites to prevent the migration of the intermediates and to form a uniform deposition layer on the SWCNT surface, which realized a higher overall charge capacity as well as a lower overpotential [49].

## Conclusion

We developed a novel cathode for the  $\text{Li}-\text{O}_2$  battery using polymer-coated SWCNTs as the electrode material and studied the effect of the coating polymer, PyPBI, on the cell performance in terms of rechargeability. As a result, the cycle stability improved by the PyPBI coating. We assumed that the coordination of  $\text{Li}^+$  to PyPBI played an important role in the favorable growth of the discharge product on SWCNT/PyPBI, which realized a smooth decomposition of the product upon charging. Our finding will lead to further ideas, such as the grafting of polyethylene oxide, known to show strong  $\text{Li}^+$  coordination, on SWCNTs, and a series of studies using a similar concept will offer advanced  $\text{Li}-\text{O}_2$  cathodes with better performances.

**Acknowledgements** This study was supported by NEDO [grant Advanced Research Program for Energy and Environmental Technologies]; MEXT [grant the Nanotechnology Platform Project]; JSPS [grant KAKENHI (JP15H01002, JP16K14084 and JP16H06056)] and JST [grant COI Program and grant PRESTO (JP16022050600)].

## Compliance with ethical standards

**Conflict of interest** The authors declare that they have no conflict of interest.

**Publisher's note:** Springer Nature remains neutral with regard to jurisdictional claims in published maps and institutional affiliations.

## References

- Lu J, Li L, Park JB, Sun YK, Wu F, Amine K. Aprotic and aqueous Li-O<sub>2</sub> batteries. *Chem Rev.* 2014;114:5611–40.
- Wang Z-L, Xu D, Xu J-J, Zhang X-B. Oxygen electrocatalysts in metal-air batteries: from aqueous to nonaqueous electrolytes. *Chem Soc Rev.* 2014;43:7746–86.
- Gao J, Cai X, Wang J, Hou M, Lai L, Zhang L. Recent progress in hierarchically structured O<sub>2</sub>-cathodes for Li-O<sub>2</sub> batteries. *Chem Eng J.* 2018;352:972–95.
- Wang K-X, Zhu Q-C, Chen J-S. Strategies toward high-performance cathode materials for lithium-oxygen batteries. *Small.* 2018;14:1800078.
- Song K, Agyeman DA, Park M, Yang J, Kang Y-M. High-energy-density metal-oxygen batteries: lithium-oxygen batteries vs Sodium-oxygen Batteries. *Adv Mater.* 2017;29:1606572.
- Li Y, Wang X, Dong S, Chen X, Cui G. Recent advances in non-aqueous electrolyte for rechargeable Li-O<sub>2</sub> batteries. *Adv Energy Mater.* 2016;6:1600751.
- Lim H-D, Lee B, Bae Y, Park H, Ko Y, Kim H, et al. Reaction chemistry in rechargeable Li-O<sub>2</sub> batteries. *Chem Soc Rev.* 2017;46:2873–88.
- Ma Z, Yuan X, Li L, Ma Z-F, Wilkinson DP, Zhang L, et al. A review of cathode materials and structures for rechargeable lithium-air batteries. *Energy Environ Sci.* 2015;8:2144–98.
- Tikekar MD, Choudhury S, Tu Z, Archer LA. Design principles for electrolytes and interfaces for stable lithium-metal batteries. *Nat Energy.* 2016;1:16114.
- Kraysberg A, Ein-Eli Y. The impact of nano-scaled materials on advanced metal-air battery systems. *Nano Energy.* 2013;2:468–80.
- Lu Y, Wen Z, Jin J, Cui Y, Wu M, Sun S. Mesoporous carbon nitride loaded with Pt nanoparticles as a bifunctional air electrode for rechargeable lithium-air battery. *J Solid State Electrochem.* 2012;16:1863–8.
- Albertus P, Girishkumar G, McCloskey B, Sánchez-Carrera RS, Kozinsky B, Christensen J, et al. Identifying capacity limitations in the Li/oxygen battery using experiments and modeling. *J Electrochem Soc.* 2011;158:A343–51.
- Lu YC, Kwabi DG, Yao KPC, Harding JR, Zhou J, Zuin L, et al. The discharge rate capability of rechargeable Li-O<sub>2</sub> batteries. *Energy Environ Sci.* 2011;4:2999–3007.
- Cui Y, Wen Z, Liu Y. A free-standing-type design for cathodes of rechargeable Li-O<sub>2</sub> batteries. *Energy Environ Sci.* 2011;4:4727–34.
- Wang Z-L, Xu D, Xu J-J, Zhang L-L, Zhang X-B. Graphene oxide gel-derived, free-standing, hierarchically porous carbon for high-capacity and high-rate rechargeable Li-O<sub>2</sub> batteries. *Adv Funct Mater.* 2012;22:3699–705.
- Mitchell RR, Gallant BM, Thompson CV, Shao-Horn Y. All-carbon-nanofiber electrodes for high-energy rechargeable Li-O<sub>2</sub> batteries. *Energy Environ Sci.* 2011;4:2952–8.
- Wang Z-L, Xu D, Wang H-G, Wu Z, Zhang X-B. In situ fabrication of porous graphene electrodes for high-performance energy storage. *ACS Nano.* 2013;7:2422–30.
- Zheng M, Jiang J, Lin Z, He P, Shi Y, Zhou H. Stable voltage cutoff cycle cathode with tunable and ordered porous structure for Li-O<sub>2</sub> batteries. *Small.* 2018;14:1803607.

19. Zhao C, Yu C, Li S, Guo W, Zhao Y, Dong Q, et al. Ultrahigh-capacity and long-life lithium–metal batteries enabled by engineering carbon nanofiber–stabilized graphene aerogel film host. *Small*. 2018;14:1803310.
20. Dai J, Kogut T, Jin L, Reisner D. Carbon nanotube electrode materials for Li-air. *Cells ECS Trans*. 2008;6:381–7.
21. Lee YJ, Park SH, Kim SH, Ko Y, Kang K, Lee YJ. High-rate and high-areal-capacity air cathodes with enhanced cycle life based on RuO<sub>2</sub>/MnO<sub>2</sub> bifunctional electrocatalysts supported on CNT for pragmatic Li–O<sub>2</sub> batteries. *ACS Catal*. 2018;8:2923–34.
22. Ni W, Liu S, Fei Y, He Y, Ma X, Lu L, et al. Preparation of carbon nanotubes/manganese dioxide composite catalyst with fewer oxygen-containing groups for Li–O<sub>2</sub> batteries using polymerized ionic liquids as sacrifice agent. *ACS Appl Mater Interfaces*. 2017;9:14749–57.
23. Nomura A, Ito K, Kubo Y. CNT sheet air electrode for the development of ultra-high cell capacity in lithium-air batteries. *Sci Rep*. 2017;7:45596.
24. Okamoto M, Fujigaya T, Nakashima N. Design of an assembly of poly(benzimidazole), carbon nanotubes, and Pt nanoparticles for a fuel-cell electrocatalyst with an ideal interfacial nanostructure. *Small*. 2009;5:735–40.
25. Kim C, Fujigaya T, Nakashima N. One-pot synthesis of gold-platinum core-shell nanoparticles on polybenzimidazole-decorated carbon nanotubes. *Chem Lett*. 2014;43:1737–9.
26. Fujigaya T, Kim C, Matsumoto K, Nakashima N. Palladium-based anion-exchange membrane fuel cell using koh-doped polybenzimidazole as the electrolyte. *ChemPlusChem*. 2014;79:400–05.
27. Okamoto M, Fujigaya T, Nakashima N. Individual dissolution of single-walled carbon nanotubes by using polybenzimidazole, and highly effective reinforcement of their composite films. *Adv Funct Mater*. 2008;18:1776–82.
28. Fujigaya T, Okamoto M, Nakashima N. Design of an assembly of pyridine-containing polybenzimidazole, carbon nanotubes and Pt nanoparticles for a fuel cell electrocatalyst with a high electrochemically active surface area. *Carbon*. 2009;47:3227–32.
29. Fujigaya T, Uchinoumi T, Kaneko K, Nakashima N. Design and synthesis of nitrogen-containing calcined polymer/carbon nanotube hybrids that act as a platinum-free oxygen reduction fuel cell catalyst. *Chem Commun*. 2011;47:6843–5.
30. Kumbharkar SC, Karadkar PB, Kharul UK. Enhancement of gas permeation properties of polybenzimidazoles by systematic structure architecture. *J Membr Sci*. 2006;286:161–9.
31. Hafez IH, Berber MR, Fujigaya T, Nakashima N. Enhancement of platinum mass activity on the surface of polymer-wrapped carbon nanotube-based fuel cell electrocatalysts. *Sci Rep*. 2014;4:6295.
32. Fujigaya T, Morita J, Nakashima N. Grooves of bundled single-walled carbon nanotubes dramatically enhance the activity of the oxygen reduction reaction. *ChemCatChem*. 2014;6:3169–73.
33. Bryantsev VS, Giordani V, Walker W, Blanco M, Zecevic S, Sasaki K, et al. Predicting solvent stability in aprotic electrolyte Li–Air batteries: nucleophilic substitution by the superoxide anion radical (O<sub>2</sub><sup>•-</sup>). *J Phys Chem A*. 2011;115:12399–409.
34. Balaish M, Kraysberg A, Ein-Eli Y. A critical review on lithium-air battery electrolytes. *Phys Chem Chem Phys*. 2014;16:2801–22.
35. Xu W, Hu J, Engelhard MH, Towne SA, Hardy JS, Xiao J, et al. The stability of organic solvents and carbon electrode in non-aqueous Li–O<sub>2</sub> batteries. *J Power Sources*. 2012;215:240–7.
36. Luntz AC, McCloskey BD. Nonaqueous Li–Air batteries: a status report. *Chem Rev*. 2014;114:11721–50.
37. Lu J, Li L, Park J-B, Sun Y-K, Wu F, Amine K. Aprotic and aqueous Li–O<sub>2</sub> batteries. *Chem Rev*. 2014;114:5611–40.
38. Zhai D, Wang H-H, Yang J, Lau KC, Li K, Amine K, et al. Disproportionation in Li–O<sub>2</sub> batteries based on a large surface area carbon cathode. *J Am Chem Soc*. 2013;135:15364–72.
39. Lin X, Zhou L, Huang T, Yu A. Hierarchically porous honeycomb-like carbon as a lithium-oxygen electrode. *J Mater Chem A*. 2013;1:1239–45.
40. Zhang SS, Foster D, Read J. Discharge characteristic of a non-aqueous electrolyte Li/O<sub>2</sub> battery. *J Power Sources*. 2010;195:1235–40.
41. McCloskey BD, Speidel A, Scheffler R, Miller DC, Viswanathan V, Hummelshøj JS, et al. Twin Problems of interfacial carbonate formation in nonaqueous Li–O<sub>2</sub> batteries. *J Phys Chem Lett*. 2012;3:997–1001.
42. Lu Y-C, Shao-Horn Y. Probing the reaction kinetics of the charge reactions of nonaqueous Li–O<sub>2</sub> batteries. *J Phys Chem Lett*. 2013;4:93–9.
43. Gallant BM, Kwabi DG, Mitchell RR, Zhou J, Thompson CV, Shao-Horn Y. Influence of Li<sub>2</sub>O<sub>2</sub> morphology on oxygen reduction and evolution kinetics in Li–O<sub>2</sub> batteries. *Energy Environ Sci*. 2013;6:2518–28.
44. Aurbach D, McCloskey BD, Nazar LF, Bruce PG. Advances in understanding mechanisms underpinning lithium–air batteries. *Nat Energy*. 2016;1:16128.
45. Mitchell RR, Gallant BM, Shao-Horn Y, Thompson CV. Mechanisms of morphological evolution of Li<sub>2</sub>O<sub>2</sub> particles during electrochemical growth. *J Phys Chem Lett*. 2013;4:1060–4.
46. Brzezinski B, Jarczewski A, Stańczyk M, Zundel G. Hydrogen and Li + bonds with guanidine substituted azo-compounds—an FT-IR study. *J Mol Struct*. 1993;297:81–6.
47. Xiao J, Mei D, Li X, Xu W, Wang D, Graff GL, et al. Hierarchically porous graphene as a lithium-air battery electrode. *Nano Lett*. 2011;11:5071–78.
48. Nakanishi S, Mizuno F, Nobuhara K, Abe T, Iba H. Influence of the carbon surface on cathode deposits in non-aqueous Li–O<sub>2</sub> batteries. *Carbon*. 2012;50:4794–803.
49. Yang Y, Shi M, Zhou Q-F, Li Y-S, Fu Z-W. Platinum nanoparticle–graphene hybrids synthesized by liquid phase pulsed laser ablation as cathode catalysts for Li-air batteries. *Electrochem Commun*. 2012;20:11–4.